DETECTING RADIO-AGN SIGNATURES IN RED GEYSERS

Namrata Roy 1† , Kevin Bundy 1,2 , Edmond Cheung 3 , Wiphu Rujopakarn 3,4 , Michele Cappellari 5 , Francesco Belfiore 1 , Renbin Yan 6 , Tim Heckman 7 , Matthew Bershady 8 , Jenny Greene 9 , Kyle Westfall 1,2 , Niv Drory 10 , Kate Rubin 11 , David Law 12 , Kai Zhang 6 , Joseph Gelfand 13,14 , Dmitry Bizyaev 15,16 , David Wake 8,17 , Karen Masters 18 , Daniel Thomas 18 , Cheng Li 3 , Rogemar A. Riffel 19,20

Draft version July 10, 2018

ABSTRACT

A new class of quiescent galaxies harboring possible AGN-driven winds has been discovered using spatially resolved optical spectroscopy from the ongoing SDSS-IV MaNGA survey. These galaxies, termed "red geysers", constitute 5 – 10% of the local quiescent population and are characterized by narrow bisymmetric patterns in ionized gas emission features. Cheung et al. argued that these galaxies host large-scale AGN-driven winds that may play a role in suppressing star formation at late times. In this work, we test the hypothesis that AGN activity is ultimately responsible for the red geyser phenomenon. We compare the nuclear radio activity of the red geysers to a matched control sample with similar stellar mass, redshift, rest frame NUV-r color, axis ratio and presence of ionized gas. We have used the 1.4 GHz radio continuum data from VLA FIRST survey to stack the radio flux from the red geyser and control samples. In addition to a 3 times higher FIRST detection rate, we find that red geysers have a 5σ higher level of average radio flux than control galaxies. After restricting to rest-frame NUV - r color > 5 and checking mid-IR WISE photometry, we rule out star formation contamination and conclude that red geysers are associated with more active AGN. Red geysers and a possibly-related class with disturbed H α emission account for 40% of all radio-detected red galaxies with log $M_{\star} < 11$. Our results support a picture in which episodic AGN activity drives large-scale-relatively weak ionized winds that may provide a feedback mechanism for many early-type galaxies.

Keywords: galaxies: evolution — galaxies: formation

- ¹ Department of Astronomy and Astrophysics, University of California, 1156 High Street, Santa Cruz, CA 95064
- ² UCO/Lick Observatory, Department of Astronomy and Astrophysics, University of California, 1156 High Street, Santa Cruz, CA 95064
- ³ Kavli Institute for the Physics and Mathematics of the Universe (WPI), The University of Tokyo Institutes for Advanced Study, The University of Tokyo, Kashiwa, Chiba 277-8583, Japan
- ⁴ Department of Physics, Faculty of Science, Chulalongkorn University, 254 Phayathai Road, Pathumwan, Bangkok 10330, Thailand
- ⁵ Sub-department of Astrophysics, University of Oxford, Denys Wilkinson Building, Keble Road, Oxford OX1 3RH
- ⁶ Department of Physics and Astronomy, University of Kentucky, 505 Rose Street, Lexington, KY 40506-0055, USA
- Center for Astrophysical Sciences, Department of Physics & Astronomy, The Johns Hopkins University, Baltimore, Maryland 21218
- ⁸ Department of Astronomy, University of Wisconsin-Madison, 475 North Charter Street, Madison, WI 53706, USA
- Department of Astrophysical Sciences, Princeton University, Prince-
- ton, NJ 08544, USA

 10 McDonald Observatory, Department of Astronomy, University of Texas at Austin, 1 University Station, Austin, TX 78712-0259, USA
- ¹¹ Harvard-Smithsonian Center for Astrophysics, 60 Garden Street, Cambridge, MA 02138, USA
- ¹² Space Telescope Science Institute, 3700 San Martin Drive, Baltimore, MD 21218, USA
 - ³ NYU Abu Dhabi, P.O. Box 129188, Abu Dhabi, UAE
- ¹⁴ Center for Cosmology and Particle Physics, New York University, Meyer Hall of Physics, 4 Washington Place, New York, NY 10003, USA
- ¹⁵ Apache Point Observatory and New Mexico State University, P.O. Box 59, Sunspot, NM, 88349-0059, USA
 - ¹⁶ Sternberg Astronomical Institute, Moscow State University, Moscow
- ¹⁷ Department of Physical Sciences, The Open University, Milton Kevnes, MK7 6AA, UK
- ¹⁸ Institute for Cosmology and Gravitation, University of Portsmouth, Dennis Sciama Building, Burnaby Road, Portsmouth PO1 3FX
- ¹⁹ Universidade Federal de Santa Maria, Departamento de Física,
- CCNE, 97105-900, Santa Maria, RS, Brazil

 20 Laboratório Interinstitucional de e-Astronomia LIneA, Rio de Janeiro, RJ, Brazil

[†] naroy@ucsc.edu

2 Roy et al.

1. INTRODUCTION

The level of star formation in galaxies is known to be bimodal (Blanton et al. 2003; Strateva et al. 2001; Kauffmann et al. 2003), with star-forming galaxies often referred to as the "blue cloud" while galaxies without significant star formation fall under the "red sequence" category. The latter quiescent population has old stellar ages (\gtrsim 6 Gyr) and short starformation timescales (\lesssim 1 Gyr; Tinsley 1979; Worthey et al. 1992; Trager et al. 2000; Thomas et al. 2005; Graves & Schiavon 2008; Conroy et al. 2014; Worthey et al. 2014; Choi et al. 2014). The abundance of these quiescent galaxies has increased by several factors since $z \sim 2$ (Bell et al. 2004; Bundy et al. 2006; Faber et al. 2007; Ilbert et al. 2010; Moustakas et al. 2013) which implies that more and more galaxies are transitioning from the blue, star forming portion of the colorcolor diagram towards the red side. The increase in the redand-dead population indicates that once galaxies shut off their star formation by some mechanism, they must stay quenched for a long time.

A permanent shut down of star formation is hard to explain, because the quiescent population possesses or can accrete sufficient gas to eventually start forming stars again. Major surveys have shown an abundance of gas in quiescent galaxies (Binette 1994; Buson et al. 1993; Demoulin-Ulrich et al. 1984), which if left to itself, should ultimately cool and form stars. This gas comes from a variety of sources like stellar mass loss from evolved stars (e.g., Mathews & Brighenti 2003; Ciotti & Ostriker 2007) or minor mergers. If all this gas formed stars, we would expect the global stellar mass density to be larger by a few factors than the observed at z=0. This implies that an additional feedback mechanism is required to maintain the suppression of star formation in galaxies on the red sequence (Benson et al. 2003).

While a number of feedback mechanisms have been proposed, including interstellar medium (ISM) heating from stellar winds (Conroy et al. 2015) and gravitational effects induced by galaxy bulges (Martig et al. 2009), the most popular explanation has been so-called radio-mode active galactic nuclei (AGN) feedback (Croton et al. 2006). It states that the central AGN in the host galaxy deposits energy into the surrounding gas, heating it or removing it altogether and thereby suppressing star formation (Binney & Tabor 1995; Ciotti & Ostriker 2001; Croton et al. 2006; Bower et al. 2006; Ciotti & Ostriker 2007; Ciotti et al. 2010; McNamara & Nulsen 2007; Cattaneo et al. 2009; Fabian 2012; Yuan & Narayan 2014; Heckman & Best 2014). Direct observational evidence for this "maintenance mode feedback" is limited to several nearby clusters (Cattaneo et al. 2009; Dunn & Fabian 2006; Fabian 1994, 2012; Fabian et al. 2006; McNamara & Nulsen 2007). Evidence for this mechanism in more typical galaxies remain elusive.

Recently, Cheung et al. (2016) discovered a new class of quiescent galaxies, referred to as "red geysers", that show interesting emission line patterns and kinematic properties which may signal AGN maintenance-mode feedback in action. Based on spatially resolved information from Sloan Digital Sky Survey-IV (SDSS-IV) Mapping Nearby Galaxies at Apache Point Observatory (MaNGA) survey (Bundy et al. 2015), this class of quiescent galaxies appears to host large scale winds of ionized gas that align with bi-symmetric enhancements in the spatial distribution of strong emission lines like $H\alpha$. Ionized emission extends throughout the entire galaxy with line ratios similar to LIER-like (Low Ionization

Emission Region) galaxies (Belfiore et al. 2016). In addition to their enhanced bisymmetric line emission, the red geysers also exhibit gas kinematics consistent with outflowing winds. The gradient of the gas velocity field aligns with the position angle of the emission pattern but is largely misaligned with the major or minor axes derived from the stellar velocity field. The gas velocity dispersion can reach $\sim 300~{\rm km~s^{-1}}$, a value that is difficult to explain by orbital motion from the galaxy's gravitational potential, considering the mass range of the galaxies.

Early-type galaxies with accreted disks, as studied by Chen et al. (2016) and Lagos et al. (2015), can show similar kinematic features as red geysers, but those features are formed due to a completely different phenomena. The accreted gas coming in from random directions begins to align with either major or minor axis through gravitational torques by the galaxy's potential well. Hence, while a misalignment in the velocity gradient of stars and gas can occur for these galaxies too, often the misalignment angle is 90° or 0°/180° depending on whether a polar disk or co-rotating/ counter rotating disk is formed. Some galaxies with accreted disks might show similar $H\alpha$ EW distributions as red geysers. Cheung et al. (2016) rejected the disk interpretation through detailed Jeans Anisotropic modeling (JAM, Cappellari 2008) of the prototypical red geyser which demonstrated that the gas velocity in this source is too high to be described by the orbital motion. Given similar high velocities and other common features shared among all the red geysers, outflowing winds emerge as a compelling interpretation (Bundy et al. in preparation), making the question of whether AGNs are capable of driving these winds particularly important.

A critical first step is to test the hypothesis that the red geyser population is more likely to host an active AGN compared to quiescent galaxies with similar global galaxy properties. For the prototypical red geyser, Cheung et al. (2016) showed that the host galaxy has a weakly and/or radiatively-inefficient supermassive black hole, accreting mass from a low-mass companion galaxy. It was detected as a central radio point source. In this paper we analyze stacked radio flux from Very Large Array (VLA) Faint Images of the Radio Sky at Twenty-Centimeters (FIRST) survey and find a higher value of radio flux from the red geyser candidates than the comparison sample of quiescent galaxies. We have excluded possible star formation contamination and/or galaxies with embedded disks from our sample.

Throughout this paper, we assume a flat cosmological model with $H_0 = 70 \text{ km s}^{-1} \text{ Mpc}^{-1}$, $\Omega_m = 0.30$, and $\Omega_{\Lambda} = 0.70$, and all magnitudes are given in the AB magnitude system.

2. DATA

2.1. MaNGA survey

Our sample comes from the ongoing SDSS-IV MaNGA survey (Blanton et al. 2017; Bundy et al. 2015; Drory et al. 2015; Law et al. 2015; Yan et al. 2016; SDSS Collaboration et al. 2016). MaNGA is an integral field spectroscopic survey that provides spatially resolved spectroscopy for nearby galaxies (z ~ 0.03) with an effective spatial resolution 2.5" (full width at half-maximum; FWHM). The MaNGA survey uses the SDSS 2.5 meter telescope in spectroscopic mode (Gunn et al. 2006) and the two dual-channel BOSS spectrographs (Smee et al. 2013) that provide continuous wavelength coverage from the near-UV to the near-IR: 3,600 – 10,000 Å. The spectral resolution varies from R \sim 1400 at 4000 Å to

 $R \sim 2600$ at 9000 Å. An r-band signal-to-noise (S/N) of 4-8 Å $^{-1}$ is achieved in the outskirts (i.e., 1-2 R $_e$) of target galaxies with an integration time of approximately 3-hr. MaNGA will observe roughly 10,000 galaxies with log $M_*/M_{\odot} \gtrsim 9$ across ~ 2700 deg 2 over its 6 yr duration. In order to balance radial coverge versus spatial resolution, MaNGA observes two thirds of its galaxy sample to ~ 1.5 R $_e$ and one third to 2.5 R $_e$. The MaNGA target selection is described in detail in Wake et al. (2017).

The raw data are processed with the MaNGA Data Reduction Pipeline (DRP) (Law et al. 2016). An individual rowby-row algorithm is used to extract the fiber flux and derive inverse variance spectra from each exposure, which are then wavelength calibrated, flat-fielded and sky subtracted. The MaNGA sample and data products we use here are drawn from the MaNGA Product Launch-5 (MPL-5) and are nearly identical to those released as part of the SDSS Data Release 14 (DR14, Abolfathi et al. (2018)). We use spectral measurements and other analyses carried out by the MaNGA Data Analysis Pipeline (DAP) which is described in Westfall et al. (in prep). In brief, the stellar-continuum fitting and stellar kinematic measurements of each "spaxel" are done using Penalised Pixel-fitting pPXF (Cappellari & Emsellem 2004; Cappellari 2017). The DAP uses templates from the MIUSCAT stellar population model libraries (Vazdekis et al. 2012) spanning a wide range in stellar age (from 60 Myr to 15 Gyr) and metallicity ([Z/H] = 0.2, 0.0, -0.4, -0.7). The strong emission lines including [OIII] $\lambda\lambda 4959,5007$, H α , [NII] $\lambda\lambda6548,83$ are fit by gaussians to derive emission line fluxes. The spectral-fitting procedure can recover line fluxes with less than 0.12 dex error for S/N > 3 for all strong lines except H β , which suffers from slightly larger errors $(\sim 0.2 \text{ dex})$ (Westfall et al. in prep.). The final output from the DAP are gas and stellar kinematics, emission line properties and stellar absorption indices.

We use ancillary data drawn from the NASA-Sloan Atlas²² (NSA) catalog which reanalyzes images and derives morphological parameters for local galaxies observed in Sloan Digital Sky Survey imaging. It compiles spectroscopic redshifts, UV photometry (from GALEX; Martin et al. 2005), stellar masses, and structural parameters.

2.2. FIRST survey

The radio data studied in this paper comes primarily from the Very Large Array (VLA) Faint Images of the Radio Sky at Twenty Centimeters (FIRST; Becker et al. 1995) survey which obtained data at frequency channels centered at 1.36 GHz and 1.4 GHz over 10,000 square degrees in the North and South Galactic Caps. The source detection threshold is ~ 1 mJy corresponding to a source density of ~ 90 sources deg $^{-2}$. FIRST images have 1.8" pixels with a resolution of ~ 5 " and typical rms of 0.15 mJy. The astrometric accuracy of each source is 0.5 – 1" at the source detection threshold. Since FIRST survey area was designed to overlap with the Sloan Digital Sky Survey (SDSS; York et al. 2000; Abazajian et al. 2009), most MaNGA targets have FIRST data coverage. However, the 1 mJy threshold results in non detections for most MaNGA galaxies.

For each pointing center, there are twelve adjacent single-field pointings that are co-added to produce the final FIRST image. Sources are extracted from the co-added re-

duced images and fit by two dimensional Gaussians to derive peak flux, integrated flux densities and size information. The current FIRST catalog is accessible from the FIRST search page²³. The full images are available in ftp://archive.stsci.edu/pub/vla_first/data.

2.3. SDSS+WISE Star formation rates

In order to assess possible contamination from obscured star formation, we have used the Chang et al. (2015) catalog to obtain IR-based star formation rates (SFR). The catalog contains 858,365 galaxies within the SDSS spectroscopic sample as compiled in the New York University Value-added Galaxy Catalog (NYU-VAGC; Blanton et al. 2005; Adelman-McCarthy et al. 2008; Padmanabhan et al. 2008) and crossmatched with the ALLWISE (Wide Field Infrared Survey Explorer) source catalog. Unlike optical emission line SFR estimates, Chang et al. (2015) utilized mid-IR data from full WISE photometry and employed an SED fitting technique to estimate stellar mass and star formation rates. Their modeling is based on the MAGPHYS library 24 (MAGPHYS contains 50,000 stellar population template spectra and 50,000 PAH+dust emission template spectra) and is applied to all z < 0.2 galaxies with good WISE photometry (FLAG_W = 1 or 2), and good-quality SED fits (FLAG_CHI2 = 1). We have used the public Chang et al. (2015) catalogs ²⁵. Details are given in Chang et al. (2015).

3. METHOD

The identification of red geysers is based on the optical resolved spectroscopic data from MaNGA. Sub-section §3.1.1 describes the conditions and criteria that have been used to select our sample. Matched control sample galaxies have been selected from the full galaxy sample via the method discussed in §3.1.2. A third category of galaxies, which we call the "H α -disturbed" class as described in §3.1.3, consists of galaxies that are not classified as geysers but show suggestive kinematic and emission line properties that may be related to the gevser phenomena. The H α -disturbed class is excluded both from the red geyser and control samples. We perform aperture photometry (described in detail in §3.2) on the FIRST radio cutouts for all galaxies using an aperture size of 10'' diameter, to obtain radio flux values and the associated photometric errors. The galaxies which satisfy the condition flux/error > 3are classified as "radio-detected" with a confidence level of 3σ . Since the detection threshold of the VLA FIRST survey is shallow (\sim 1 mJy), many galaxies might lie just below the sensitivity limit. Section §3.2 describes the stacking analysis that allows us to constrain the average radio flux for samples of galaxies that are undetected individually. The medianstacked FIRST images provide greater signal-to-noise with typical rms $\approx 10 \ \mu Jy$.

3.1. Sample Selection

In this section we describe the identification of red geysers, the selection of matched control sample galaxies and discovery of the $H\alpha$ -disturbed galaxies.

3.1.1. Red geysers

Red geysers are visually selected based on their characteristic features, as described in Cheung et al. (2016). Red geysers

²² http://www.nsatlas.org

²³ http://sundog.stsci.edu/cgi-bin/searchfirst

²⁴ http://www.iap.fr/magphys/

²⁵ http://irfu.cea.fr/Pisp/yu-yen.chang/sw.html

have red colors defined by rest frame color NUV - r > 5. The specified UV-optical color cut selects predominantly quiescent galaxies (Salim et al. 2005, 2007, 2009). The red geysers must show narrow bi-symmetric patterns in the ionized gas emission as observed in the equivalent width (EW) maps of strong emission lines like $H\alpha$ and [OIII]. These patterns should line up approximately with the gaseous kinematic axis, but we pay close attention to cases where the mis-alignment of the stellar and gas velocity field is 0°, 180° or 90° in order to exclude embedded co-rotating, counter-rotating and polar gas disks. Another important defining property of the red geysers is that they have high absolute values of gas velocities $(\sim 250-300 \text{ km s}^{-1})$ compared to stellar velocities, as well as high gas velocity dispersion values ($\sim 200 \text{ km s}^{-1}$). Hence the observed second velocity moments $(V_{\rm rms} \equiv \sqrt{V^2 + \sigma^2})$ of the ionized gas should largely exceed the second velocity moments of the stars, suggesting that the ionized gas kinematics in these galaxies cannot be explained by gravitationallybound orbits alone. A typical example of a red geyser is shown in Fig 1. Further details will be described in Bundy at al. (in prep).

Accreted gas disks in early type galaxies (e.g., Chen et al. 2016) can sometimes produce similar gas velocity gradients like the red geysers, due to rotation of the gaseous material in the disk. A few edge-on disks show a bisymmetric pattern in EW map similar to the red geysers. Hence, we include a few extra steps in our visual identification, to exclude galaxies with a visible disk component or dust lanes apparent in the optical SDSS image. We discard edge-on galaxies with axis ratio b/a < 0.3. We checked the galaxy specific stellar angular momentum (λ_{Re}) and ellipticity (ϵ) from the extensive catalog in Graham et al. (2018). We find that 95% of the red geysers are fast rotator early-type galaxies. Our control sample galaxies are of similar nature, 97% of which are fast rotators according to Graham et al. (2018). Since the fast rotators have stellar disks and are axisymmetric, this implies that a gas disk cannot be in equilibrium if it is misaligned with the stellar kinematic PA.

In addition, any galaxy showing a very low value of average gas velocity dispersion through out the galaxy (< 60 km s⁻¹ which is roughly the average dispersion value observed in polar disks), has been discarded from our red geyser sample. As described in Cheung et al. (2016), the gas velocity fields of the red geysers are poorly fit by flexible disk rotation models and the line ratios from ionized gas land either in the LINER or AGN region in the BPT diagram.

Currently, our sample has 84 red geysers, which accounts for $\approx 8\%$ of quiescent MaNGA galaxies (defined as NUV – r > 5, see Section §3.1.2).

3.1.2. Control Sample

We create a control sample of quiescent galaxies with NUV - r > 5 (shown in Fig 2), which are matched in global properties but do not show the resolved geyser-like features described in §3.1.1.

For each red geyser, we match up to five unique quiescent galaxies with the following criteria:

- $\begin{array}{l} \bullet \hspace{0.2cm} |\hspace{0.05cm} \log \hspace{0.05cm} M_{*,\hspace{0.1cm} \mathrm{red}\hspace{0.1cm} \mathrm{geyser}}/M_{*,\hspace{0.1cm} \mathrm{control}}| < 0.2 \hspace{0.05cm} \mathrm{dex} \\ \bullet \hspace{0.1cm} |\hspace{0.05cm} z_{\mathrm{red}\hspace{0.1cm} \mathrm{geyser}} z_{\mathrm{control}}| < 0.01 \\ \bullet \hspace{0.1cm} |\hspace{0.05cm} b/a_{\mathrm{red}\hspace{0.1cm} \mathrm{geyser}} b/a_{\mathrm{control}}| < 0.1, \end{array}$

where M_* is the stellar mass, z is the spectroscopic redshift, and b/a is the axis ratio from the NSA catalog. Stellar mass

and redshift have been shown to correlate with radio emission and thus must be controlled for (e.g., Condon 1984; Dunlop & Peacock 1990; Best et al. 2005). We also control for axis ratio so that we do not compare potentially dust-reddened edge-on galaxies with the relatively face-on red geyser galaxies. This matching technique results in ~ 300 unique control galaxies. Fig 3 shows an example of a typical quiescent galaxy from the control sample.

Fig. 4 compares the global galaxy properties of the control sample and the red geysers. The red geysers (red) and the control sample (blue) are well-matched in all four parametersstellar mass, redshift, color and axis ratio as expected.

3.1.3. $H\alpha$ -Disturbed Galaxies

During the course of visual inspection, we have discovered another category of galaxies which we will hereby refer to as "H α -disturbed". Fig 5 shows an example. The gas content of these galaxies is high (median H α equivalent width (EW) value > 0.5 Å similar to ~ 0.8 Å in the red geysers) but the $H\alpha$ equivalent width maps don't show the clear bisymmetric patterns of a red geyser. They show twisted, disturbed H α EW maps, sometimes with individual blobs of gas that are found throughout the galaxy. Some have high gas velocity dispersion, upwards of $\sim 200 \text{ km s}^{-1}$ as seen in red geyser population. We found 60 such "H α -disturbed" candidates which we treat as a separate third category and remove from both the red geyser and control samples.

3.2. FIRST Radio Photometry and Stacking

To obtain the radio flux, we perform aperture photometry on the FIRST cutouts for our sample of 84 red geysers, ~ 300 control galaxies and 60 disturbed galaxies. We first determine which FIRST tile (of dimension $34.5' \times 46.5'$) a specific galaxy falls on. If a galaxy is located too close to the FIRST tile edge (less than 10''), that galaxy is discarded. We extract a small cutout 50×50 pixels wide (each pixel is 1.8") centered on the galaxy of interest. We use a circular aperture of 10" diameter centered on the galaxy and sum the radio flux values within. The photometric error (σ_{phot}) is calculated by repeating this procedure for 100 random positions inside the FIRST tile. We take the standard deviation of the resulting distribution to obtain an error value specific to a particular tile. We have defined the criteria for radio detection to be flux/error > 3. We then perform a median stack of the FIRST images associated with the three samples described in §3.1. To ensure that our results are not biased by a few radio bright sources, we have made separate radio stacks with the individually radio detected sources removed.

We have also tested that our stacked radio signal is not an artifact of faulty FIRST tiles by median stacking random cutouts within a radius of 75" in the same FIRST tile where the galaxy is located. We would expect these "blank" stacks to have pure white noise with no radio signal.

Fig. 6 shows the images of the median radio stacks of these four samples — (1) the red geysers, (2) the control sample, (3) the non-radio-detected red geysers, and (4) the non-radiodetected control sample. The rightmost panel in both the rows show the blank stacks. Reassuringly, the blank stacks show no

We perform additional separate stacks controlling for ionized gas content and star formation rates in the control galaxies to see their effect on the radio output. Details of our findings are given in §4.

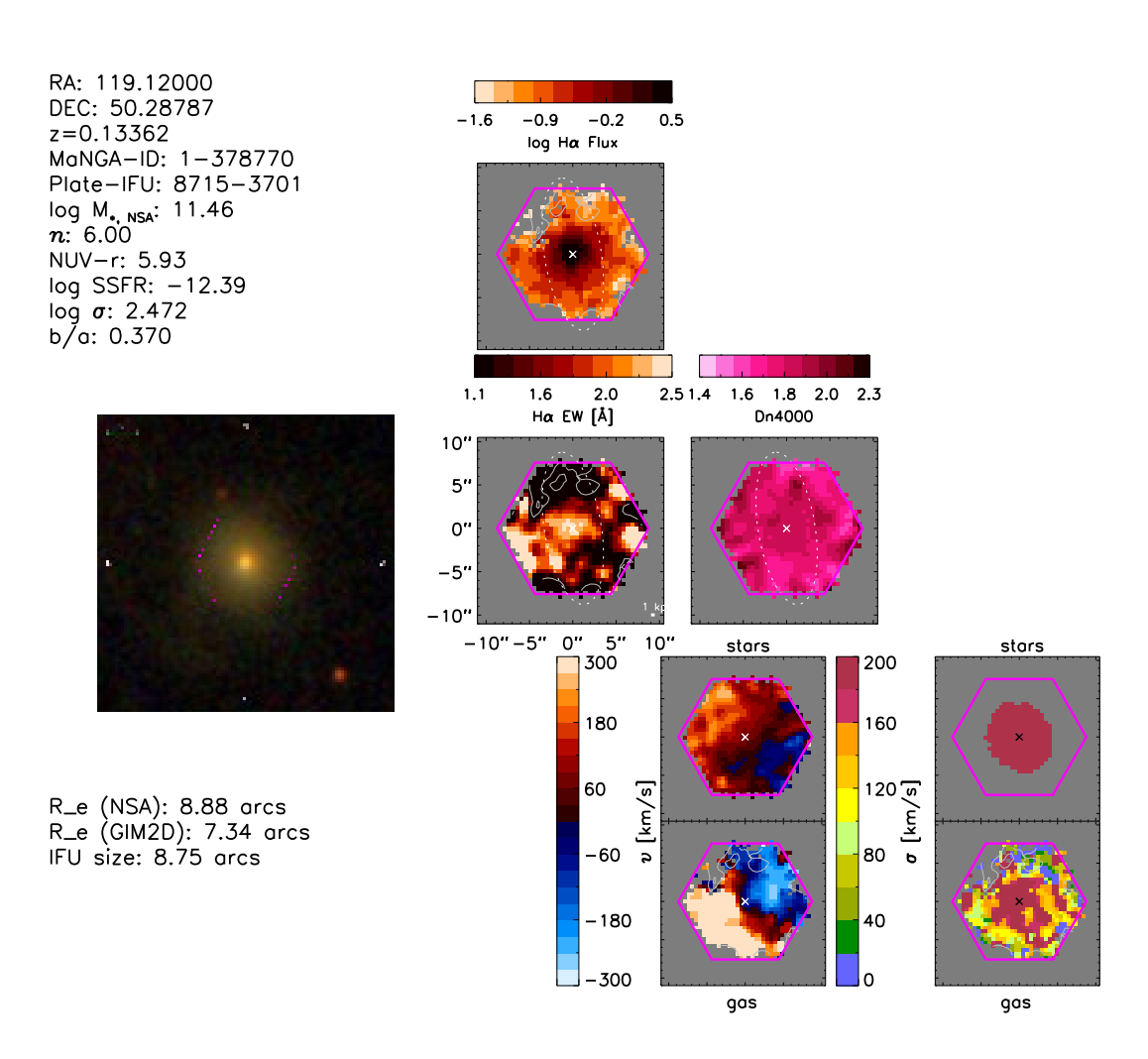


Figure 1. A typical red geyser included in our sample. The data has been obtained from MaNGA Integral Field spectroscopic observations. The panel on the left shows the optical image of the galaxy (MaNGA-ID: 1-634825). The magenta hexagon marked in the image is the extent of the MaNGA fiber bundle. On the right, as labelled, we have shown the $H\alpha$ -flux map, Equivalent width map, Dn4000 absorption map, the velocity maps of gas and the stars along with their dispersion. As described in §3.1.1, this galaxy satisfies all the conditions that we use to classify an object as red geyser. Specially notable is the bi-symmetric pattern in the equivalent width map of $H\alpha$ and the kinematic axis align perfectly with the gas velocity field.

6 Roy et al.

In order to account for the systematic error due to sample construction, we perform a bootstrap analysis on all our samples. We construct 1000 random samples with replacement with the same size as each sample and compute the stacked radio flux as before. We call the standard deviation of the resulting flux distributions $\sigma_{\rm sys}$. The final error is then computed by adding the photometric error and systematic error in quadrature $\sigma = \sqrt{\sigma_{\rm phot}^2 + \sigma_{\rm sys}^2}$

4. RESULTS

4.1. Radio detection of red geysers vs. control sample

We have crossmatched FIRST radio detections with our sample of red geysers and control galaxies. Among the red geysers, 12 out of 84 (\sim 15%) are found to be radio-detected with standard deviation \sim 3.5. Among the control sample, 14 out of 260 are detected ($\sim 5\%$) with standard deviation \sim 4. Red geysers show a higher radio detection rate compared to our control sample with a significance level of 5σ . We also find that the red geysers make up an appreciable fraction $(\sim 10\%)$ of the red MaNGA galaxies which are radio-detected by FIRST survey. This fraction increases to $\sim 20\%$ when the disturbed category galaxies are included along with the red geyser population. If we limit our sample to log $M_{\star} < 11$, the detection rate of red geysers and $H\alpha$ -disturbed goes up to 40%. The various detection statistics are very similar if we use the catalog of radio detected sources from Best & Heckman (2012).

We have also followed up 10 red geyser candidates with 30′ Jansky-VLA observations in the A-array configuration. We detect 9 out of 10 sources with JVLA, all consistent with nuclear point-sources given the 0.3″ beam size.

4.2. Stacked radio activity of red geysers vs. the control sample

Fig 7 shows the first main result of our analysis. We compare the median radio stacks of the red geysers (red circles) with that of the control sample (blue circles). The plot is a one-dimensional figure whose x-axis gives the information about the type of sample while the y-axis shows the median-stacked flux value along with 1σ error bars. Data points in the column marked "All" indicate the median fluxes when the entire sample of geysers and control samples are included in the stack. In the column labelled "Radio non-detection" we have excluded radio bright red geysers and control galaxies. We see that for both these cases, the red geyser radio stacks are higher than the control sample at greater than 99.99% confidence (> 5σ).

We additionally control for the presence of ionized gas in our sample. We obtain $H\alpha$ equivalent width (EW) measurements from the MaNGA DAP. The mean value obtained by averaging the EW ($H\alpha$) values of all spaxels in a particular galaxy within 1.5 effective radii is used as the mean EW value, and a proxy for ionized gas content. The control galaxies show an average value of 0.3 Å, somewhat lower than the corresponding 0.8 Å seen in the red geyser sample. To compare against galaxies with similar equivalent width values, we select an additional control sample with EW > 0.5 Å (stacks marked with yellow points). Fig 7 shows the corresponding stacked flux in yellow; "All" and "Radio Non-detections" implies whether the sample includes radio-detected sources. We see that even the radio stack of control galaxies having a comparable level of ionized gas, has a value about 3 times less

than that of the red geyser stack. In addition to that, the stacked radio flux for the control galaxies with gas doesn't show much difference for "All" and "Radio Non-detections" sample, which implies that presence of higher amount of ionized gas in the control sample doesn't necessarily affect the radio-detection rate.

The detailed implications of these findings are summarized in §5.

4.3. Dusty star-formation

As described in §3.1.1, we set a color cut of rest frame NUV-r>5, and exclude edge on galaxies with b/a<0.3 to avoid possible radio contamination from star formation. However, UV wavelengths are susceptible to dust attenuation and may not reveal heavily obscured star formation (e.g., Calzetti 2001). Here we use the SDSS+WISE Chang et al. (2015) catalog for obtaining star formation rates (SFR) based on IR fluxes that are sensitive to dusty star formation. Chang et al. (2015) has utilized the full WISE photometry to model the SEDs in optical through mid-IR bands and obtained updated measures of mass and SFR.

Fig 8 and Fig 9 show the log SFR vs log M_{\star} and log sSFR vs log M_{\star} diagrams of the galaxies from the Chang et al. (2015) catalog. We see that the majority of red geyser and control galaxies lie in the non-star forming region, with low values of SFR and sSFR. To ensure that our result is not affected by radio contamination from dusty star formation, we have redone the stacking analysis after excluding galaxies that have log SFR $> -2M_{\odot}/\text{yr}$. This cut removes 3 red geysers and 30 control sample galaxies. Fig 10 shows the median stacked radio flux in the column labelled "Non-Starforming". We conclude that our results are not affected by contamination from dusty star formation.

WISE colors can be used to detect strong nuclear heating associated with bright AGNs or quasars at the center of the host galaxy. According to Yan et al. (2013), W1 (3.4 μ m) – W2 (4.6 μ m) > 0.8 presents an efficient mid-IR color based selection criteria for luminous AGN. Most of the red geysers have 0.6 < W1 – W2 < 0.7 with very few (1 or 2) having a value > 0.8. This lends confidence to the ability of the WISE data to constrain obscured star formation in these galaxies.

4.4. Stacked flux of $H\alpha$ -Disturbed category

In Fig 10, the stacked flux for the galaxies in the disturbed category is shown in magenta. Remarkably these galaxies show a slightly higher value of median stacked radio flux than the red geysers. The disturbed EW maps and high gas velocity dispersions revealed by MaNGA data correlate with enhanced radio flux. We will discuss the implication of this finding in Section §5.

5. DISCUSSIONS & CONCLUSION

We have performed a radio stacking analysis of 84 red geysers selected from MaNGA MPL-5 sample and have compared their median radio flux with similar quiescent nongeyser galaxies. The red geyser galaxies show significantly higher radio output than the control galaxies. We have made several subdivisions based on different physical criteria, to check our results:

- We have performed the stacking for all galaxies both in the red geyser and control samples.
- We have performed the stacking for samples in which the radio detected sources are removed so that a few

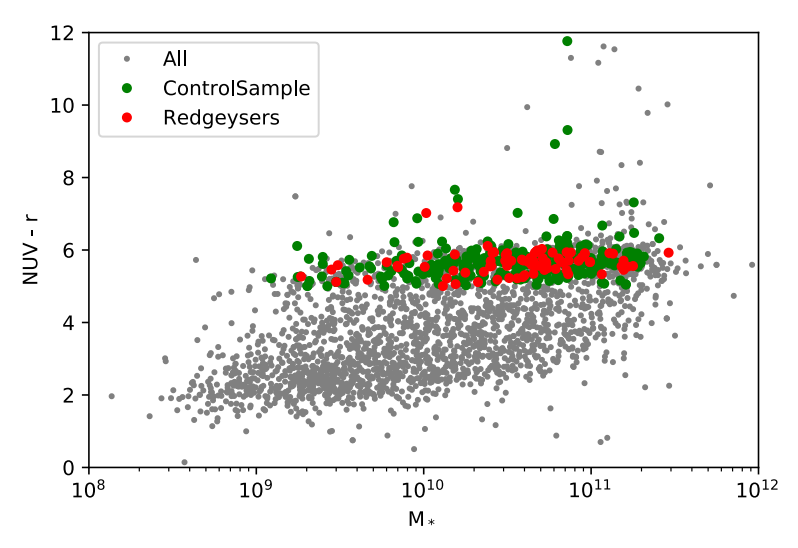


Figure 2. The rest-frame NUV-r color vs. stellar mass (log M_*) diagram of the MaNGA sample, with the red geysers in red and the control galaxies in green. Quiescent galaxies are clustered in the upper peak of the NUV-r distribution; we define NUV-r>5 as a conservative boundary of quiescent galaxies. Galaxies with NUV-r>8 are undetected in the NUV data.

8 Roy et al.

bright sources do not dominate the median stacked radio flux value.

- We have performed the stacking for galaxies with similar levels of ionized gas by imposing a cut on EW (Hα) value.
- We have performed the stacking for samples that exclude galaxies which show a high value of star formation from SDSS+WISE.

In all cases red geysers exhibit elevated radio flux values. Given our conservative NUV-r color cut and the use of WISE mid-IR data (§4.3), we can rule out star formation as the explanation for this enhanced radio flux. The other most likely sources are AGN activity or Supernova remnants. SN Ia remnants can induce radio synchrotron emission from shock-accelerated cosmic rays. However in our case, they are unlikely to be responsible for the increased radio signal in red geyser sample because our selection criteria do not involve any factors that may enhance or suppress the SN Ia rate. We have controlled primarily for the M_* and rest-frame NUV-r color, which are proxies for the B-band luminosity and age of the galaxy respectively. Thus there should be no difference in the frequency of SN Ia remnants between the red geysers and the control sample.

We followed up 10 red geysers with Jansky Very Large Array (JVLA) which have better spatial resolution and sensitivity. The presence of a nuclear radio point source is confirmed in 9 of them. We conclude that the enhanced radio emission of red geysers is due to the presence of radio-mode AGNs. The AGN feedback can induce radio emission through their radio jets (Zensus 1997; Falcke & Biermann 1999), their advection-dominated accretion flows (ADAFs; Narayan et al. 1995, 2000), and/or their winds (Jiang et al. 2010).

It stands to reason that the AGNs in the red geysers may act as the central powerhouse driving the ionized gas winds that signal the red geyser phenomenon.

It is interesting to consider how the H α -disturbed galaxies fit in this context. These galaxies show a comparable (within uncertainty) or a slightly higher value of stacked radio flux compared to the red geysers. All of them show significant gas blobs in the H α EW maps. Some of them can be potential geyser candidates or relics from mergers or tidal interactions with other galaxies. The complex gas morphology might be a product of a multi-phase and clumpy interstellar medium, ionized by the central AGN. These blobs may form out of the geyser wind material after the central engine shuts down. They may also result from a less stable accreting source. Given the uncollimated and chaotic distribution of ionized gas, it seems unlikely that cool inflowing of material from a galactic encounter is responsible. There is also no indication that that $H\alpha$ -disturbed galaxies have recently undergone a merger or interaction. Clearly more work is needed to understand them.

We would also like to highlight the handful of control galaxies with clear radio detections that are not classified as red geysers or as $H\alpha$ -disturbed. These galaxies likely host a central active nucleus and exhibit significant emission line flux. They may mean any of the following:

 Our red geyser sample based on visual inspection is not a complete sample of AGN-driven ionized winds. Red geysers may be a special type of AGN wind phenomena.

- The AGNs in the control sample are too weak too drive out sufficient gas for detection at large radii.
- A time lag may exist between AGN triggering and the development of a large-scale wind. Those AGN hosted control galaxies may not be in the red geyser phase at the current epoch, but may have passed through this phase in the past, or might in the future.

Fig 11 shows the variation of radio Luminosity ($L_{1.4 GHz}$) with stellar mass (M_{\star}) for all the FIRST radio-detected quiescent galaxies in MaNGA sample. We see that radio-AGN in the galaxies showing optical emission line features (red geysers and $H\alpha$ -disturbed) are found mostly at $\log M_{\star} < 11$ while the radio detection rate overall seems to increase above $\log M_{\star} > 11$. One possibility is that red geysers and "radio galaxies" represent different AGN populations with different associated accretion histories and fueling mechanisms. Alternatively, the declining presence of wide-scale ionized gas at higher stellar mass (Belfiore et al. 2017) may simply hide the existence of AGN-driven winds at higher masses.

We can gain further insight by considering the average luminosities from our stacked samples in two stellar mass bins. Using the median redshift in each bin, we overplot the average luminosity of red geysers and $H\alpha$ -disturbed galaxies on Fig 11. The average luminosity has been obtained from the stacked radio flux that includes both radio-detected and non-detected sources. While radio-detected sources show a strong mass dependence, the radio luminosity associated with red geysers and $H\alpha$ -disturbed galaxies increases comparatively weakly with stellar mass. This suggests that a different kind of accretion physics may be at play.

Considering the two red geyser mass bins in Fig 11, we see that the typical radio power of the red geysers is $\sim 10^{21} \, \mathrm{W \ Hz^{-1}} (\mathrm{shown \ in \ Fig \ 11 \ by \ the \ two \ black \ filled \ cir-}$ cles). From the best-fit linear relation between jet mechanical energy and the radio power from Heckman & Best (2014), we get an estimate of the jet kinetic energy to be 3×10^{41} erg/s. The AGNs in the red geysers are low-luminosity sources and their mechanical energy will be confined predominantly to size-scales of the host galaxy halo. If we assume that the observed fraction of red geysers and H α -disturbed galaxies represents their "duty cycle", then these phenomena are present 20% of the time. Multiplying this duty cycle by the typical jet kinetic power yields $\sim 6 \times 10^{40}$ erg/s, an estimate of the AGN power averaged over long time scales. We can compare this to the cooling rate implied from the X-ray gas in this stellar mass range (Best et al. 2006; O'Sullivan et al. 2001), which is similar, $\sim 5 \times 10^{40}$ erg/s. This similarity provides further evidence that red geysers may play an energetically interesting role in the suppression of gas cooling and star formation at late times.

NR thanks Professor Puragra Guhathakurta for helpful comments and discussions. RAR acknowledges CNPq and FAPERGS.

Funding for the Sloan Digital Sky Survey IV has been provided by the Alfred P. Sloan Foundation, the U.S. Department of Energy Office of Science, and the Participating Institutions. SDSS-IV acknowledges support and resources from the Center for High-Performance Computing at the University of Utah. The SDSS web site is www.sdss.org.

SDSS-IV is managed by the Astrophysical Research

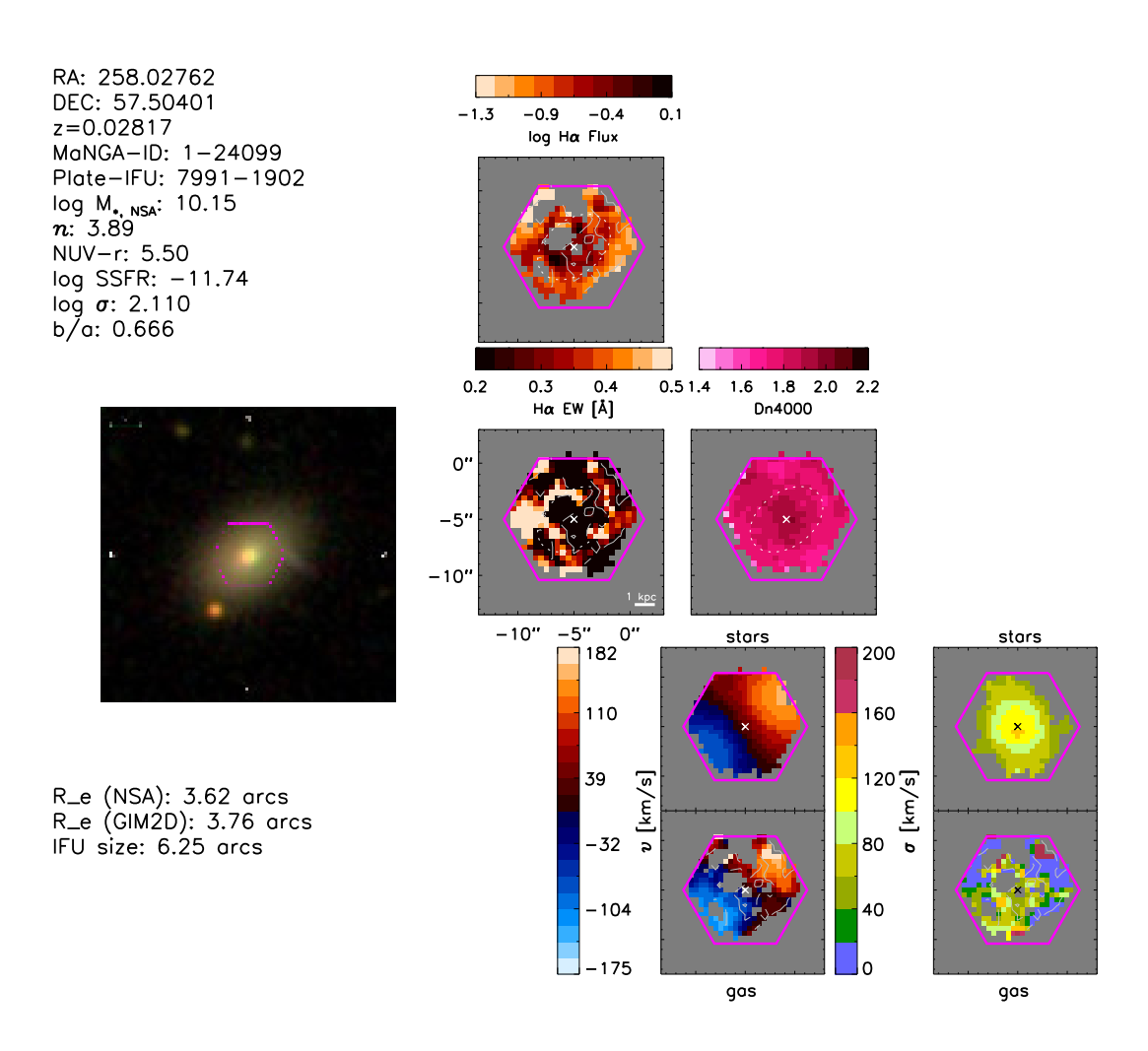


Figure 3. A typical control galaxy chosen in our sample. The data has been obtained from MaNGA Integral Field spectroscopic observations. The panel on the left shows the optical image of the galaxy (MaNGA-ID: 1-24099). The magenta hexagon marked in the image is the extent of the MaNGA fiber bundle. On the right, as labelled, we have shown the $H\alpha$ -flux map, Equivalent width map, Dn4000 absorption map, the velocity maps of gas and the stars along with their dispersion. As described in §3.1.2, this galaxy is red with NUV-r > 5, has a very low value of star formation and it is relatively face-on with b/a > 0.3. This galaxy is clearly not a red geyser as it doesn't satisfy any of the red geyser features described in §3.1.1, so it can safely be included in the control sample.

Consortium for the Participating Institutions of the SDSS Collaboration including the Brazilian Participation Group, the Carnegie Institution for Science, Carnegie Mellon University, the Chilean Participation Group, the French Participation Group, Harvard-Smithsonian Center for Astrophysics, Instituto de Astrofísica de Canarias, The Johns Hopkins University, Kavli Institute for the Physics and Mathematics of the Universe (IPMU) / University of Tokyo, the Korean Participation Group, Lawrence Berkeley National Laboratory, Leibniz Institut für Astrophysik Potsdam (AIP), Max-Planck-Institut für Astronomie (MPIA Heidelberg), Max-Planck-Institut für Astrophysik (MPA Garching), Max-Planck-Institut für Extraterrestrische Physik (MPE), National Astronomical Observatories of China, New Mexico State University, New York University, University of Notre Dame, Observatário Nacional / MCTI, The Ohio State University, Pennsylvania State University, Shanghai Astronomical Observatory, United Kingdom Participation Group, Universidad Nacional Autónoma de México, University of Arizona, University of Colorado Boulder, University of Oxford, University of Portsmouth, University of Utah, University of Virginia, University of Washington, University of Wisconsin, Vanderbilt University, and Yale University.

REFERENCES

```
Abazajian, K. N., Adelman-McCarthy, J. K., Agüeros, M. A., et al. 2009,
  ApJS, 182, 543
Abolfathi, B., Aguado, D. S., Aguilar, G., et al. 2018, ApJS, 235, 42
Acero, F., Ackermann, M., Ajello, M., et al. 2015, ApJS, 218, 23, (3FGL)
Adelman-McCarthy, J. K., Agüeros, M. A., Allam, S. S., et al. 2008, ApJS,
Atwood, W. B., Abdo, A. A., Ackermann, M., et al. 2009, ApJ, 697, 1071
Baldi, R. D., Capetti, A., & Giovannini, G. 2015, A&A, 576, A38
Barro, G., Faber, S. M., Pérez-González, P. G., et al. 2013, ApJ, 765, 104
Becker, R. H., White, R. L., & Helfand, D. J. 1995, ApJ, 450, 559
Belfiore, F., Maiolino, R., Bundy, K., et al. 2015, MNRAS, 449, 867
Belfiore, F., Maiolino, R., Maraston, C., et al. 2016, MNRAS, 461, 3111
Belfiore, F., Maiolino, R., Maraston, C., et al. 2017, MNRAS, 466, 2570
Bell, E. F., Wolf, C., Meisenheimer, K., et al. 2004, ApJ, 608, 752
Benson, A. J., Bower, R. G., Frenk, C. S., et al. 2003, ApJ, 599, 38
Best, P. N., Kauffmann, G., Heckman, T. M., et al. 2005, MNRAS, 362, 25
```

MNRAS, 368, L67 Best, P. N., & Heckman, T. M. 2012, MNRAS, 421, 1569 Binette, L., Magris, C. G., Stasinska, G. 1994, å, 292, 13

Binney, J., & Tabor, G. 1995, MNRAS, 276, 663

Blanton M. R. et al., 2003, ApJ, 594, 186

Blanton, M. R., Schlegel, D. J., Strauss, M. A., et al. 2005, AJ, 129, 2562

Blanton, M. R., Bershady, M. A., Abolfathi, B., et al. 2017, AJ, 154, 28 Bower, R. G., Benson, A. J., Malbon, R., et al. 2006, MNRAS, 370, 645

Bundy, K., Ellis, R. S., Conselice, C. J., et al. 2006, ApJ, 651, 120

Best, P. N., Kaiser, C. R., Heckman, T. M., & Kauffmann, G. 2006,

Bundy, K., Bershady, M. A., Law, D. R., et al. 2015, ApJ, 798, 7 Buson, L. M., Sadler, E. M., Zeilinger, W. W., et al. 1993, A&A, 280, 409 Calzetti, D. 2001, PASP, 113, 1449

Cappellari, M., & Emsellem, E. 2004, PASP, 116, 138

Cappellari, M. 2008, MNRAS, 390, 71

Cappellari, M. 2017, MNRAS, 466, 798

Cattaneo, A., Faber, S. M., Binney, J., et al. 2009, Nature, 460, 213

Chang, Y.-Y., van der Wel, A., da Cunha, E., & Rix, H.-W. 2015, ApJS, 219,

Chen, Y., Shi, Y., Tremonti, C. a., et al. 2016, Nature, 713, 269

Cheung, E., Faber, S. M., Koo, D. C., et al. 2012, ApJ, 760, 131

Cheung, E., Bundy, K., Cappellari, M., et al. 2016, Nature, 533, 504

Choi, J., Conroy, C., Moustakas, J., et al. 2014, ApJ, 792, 95

Cid Fernandes, R., Stasińska, G., Mateus, A., & Vale Asari, N. 2011, MNRAS, 413, 1687

Ciotti, L., D'Ercole, A., Pellegrini, S., & Renzini, A. 1991, ApJ, 376, 380

Ciotti, L., & Ostriker, J. P. 1997, ApJ, 487, L105

Ciotti, L., & Ostriker, J. P. 2001, ApJ, 551, 131

Ciotti, L., & Ostriker, J. P. 2007, ApJ, 665, 1038

Ciotti, L., Ostriker, J. P., & Proga, D. 2010, ApJ, 717, 708 Condon, J. J. 1984, ApJ, 287, 461

Condon, J. J., Cotton, W. D., Greisen, E. W., et al. 1998, AJ, 115, 1693

Conroy, C., Graves, G. J., & van Dokkum, P. G. 2014, ApJ, 780, 33

Conroy, C., van Dokkum, P. G., & Kravtsov, A. 2015, ApJ, 803, 77

Croton, D. J., Springel, V., White, S. D. M., et al. 2006, MNRAS, 365, 11 Demoulin-Ulrich, M.-H., Butcher, H. R., & Boksenberg, A. 1984, ApJ, 285,

Drory, N., MacDonald, N., Bershady, M. A., et al. 2015, AJ, 149, 77 Dunlop, J. S., & Peacock, J. A. 1990, MNRAS, 247, 19

Dunn, R. J. H., & Fabian, A. C. 2006, MNRAS, 373, 959

Faber, S. M., Willmer, C. N. A., Wolf, C., et al. 2007, ApJ, 665, 265

Fabian, A. C. 1994, ARA&A, 32, 277 Fabian, A. C., Sanders, J. S., Taylor, G. B., et al. 2006, MNRAS, 366, 417

Fabian, A. C. 2012, ARA&A, 50, 455

Falcke, H., & Biermann, P. L. 1999, A&A, 342, 49

Fang, J. J., Faber, S. M., Koo, D. C., & Dekel, A. 2013, ApJ, 776, 63

Graham, M. T., Cappellari, M., Li, H., et al. 2018, arXiv:1802.08213

Graves, G. J., & Schiavon, R. P. 2008, ApJS, 177, 446-464

Gunn, J. E., Siegmund, W. A., Mannery, E. J., et al. 2006, AJ, 131, 2332

Heckman, T. M., & Best, P. N. 2014, ARA&A, 52, 589

Hopkins, P. A., Hernquist, L., Cox, T. J. et al. 2005, ApJ, 630, 705 Ilbert, O., Salvato, M., Le Floc'h, E., et al. 2010, ApJ, 709, 644

Jiang, Y.-F., Ciotti, L., Ostriker, J. P., & Spitkovsky, A. 2010, ApJ, 711, 125

Kauffmann G. et al. 2003, MNRAS, 341, 33 Lagos, C. P., Crain, R. A., Schaye, Joop et al. 2015, MNRAS, 452, 3815

Law, D. R., Yan, R., Bershady, M. A., et al. 2015, AJ, 150, 19

Law, D. R., Cherinka, B., Yan, R., Bershady, et al. 2016, AJ, 152, 83 Lin, Y.-T., & Mohr, J. J. 2007, ApJS, 170, 71

Maraston, C., & Str'omb'ack, G. 2011, MNRAS, 418, 2785

Maraschi, L., Ghisellini, G., & Celotti, A. 1992, ApJ, 397, L5

Martig, M., Bournaud, F., Teyssier, R., & Dekel, A. 2009, ApJ, 707, 250

Martin, D. C., Fanson, J., Schiminovich, D., et al. 2005, ApJ, 619, L1

Mathews, W. G., & Brighenti, F. 2003, ARA&A, 41, 191

Matteo, T. D., Springel, V., & Hernquist, L. 2005, Nature, 433, 604

McNamara, B. R., & Nulsen, P. E. J. 2007, ARA&A, 45, 117

Moutard, T., Arnouts, S., Ilbert, O., et al. 2016, å, 590, 102

Moustakas, J., Coil, A. L., Aird, J., et al. 2013, ApJ, 767, 50 Nagar, N. M., Falcke, H., & Wilson, A. S. 2005, A&A, 435, 521

Narayan, R., Yi, I., & Mahadevan, R. 1995, Nature, 374, 623

Narayan, R., Igumenshchev, I. V., & Abramowicz, M. A. 2000, ApJ, 539,

Nyland, K., Young, L. M., Wrobel, J. M., et al. 2016, MNRAS, 458, 2221 Oke, J. B., & Gunn, J. E. 1983, ApJ, 266, 713

O'Sullivan, E., Forbes, D. A., & Ponman, T. J. 2001, MNRAS, 328, 461 Padmanabhan, N., Schlegel, D. J., Finkbeiner, D. P., et al. 2008, ApJ, 674, 1217

Rawlings, S., Saunders, R., Eales, S. A., & Mackay, C. D. 1989, MNRAS, 240, 701

Rawlings, S., & Saunders, R. 1991, Nature, 349, 138

Salim, S., Charlot, S., Rich, R. M., et al. 2005, ApJ, 619, L39

Salim, S., Rich, R. M., Charlot, S., et al. 2007, ApJS, 173, 267

Salim, S., Dickinson, M., Michael Rich, R., et al. 2009, ApJ, 700, 161

Sarazin, C. L. 1986, Reviews of Modern Physics, 58, 1

Sarzi, M., Falcón-Barroso, J., Davies, R. L., et al. 2006, MNRAS, 366, 1151

Sarzi, M., Shields, J. C., Schawinski, K., et al. 2010, MNRAS, 402, 2187 SDSS Collaboration, Albareti, F. D., Allende Prieto, C., et al. 2016,

arXiv:1608.02013

Sikora, M., Begelman, M. C. & Rees, M. J. 1994, ApJ, 421, 153

Simard, L., Mendel, J. T., Patton, D. R., et al. 2011, ApJS, 196, 11

Singh, R., van de Ven, G., Jahnke, K., et al. 2013, A&A, 558, A43 Smee, S. A., Gunn, J. E., Uomoto, A., et al. 2013, AJ, 146, 32

Stoughton, C., Lupton, R. H., Bernardi, M., et al. 2002, AJ, 123, 485

Strateva, I., Ivezic, Z., Knapp G. R., et al. 2001, AJ, 122, 1861

Tadhunter, C. 2016, A&A Rev., 24, 10

Thomas, D., Maraston, C., Bender, R., & Mendes de Oliveira, C. 2005, ApJ, 621, 673

Tinsley, B. M. 1979, ApJ, 229, 1046

Trager, S. C., Faber, S. M., Worthey, G., & González, J. J. 2000, AJ, 120,

Vazdekis, A., Ricciardelli, E., Cenarro, A. J., et al. 2012, MNRAS, 424, 157 Wake, D. A., Bundy, K., Diamond-Stanic, A. M., et al. 2017, AJ, 154, 86

White, R. L., Becker, R. H., Helfand, D. J., & Gregg, M. D. 1997, ApJ, 475,

Willott, C. J., Rawlings, S., Blundell, K. M., & Lacy, M. 1999, MNRAS, 309, 1017

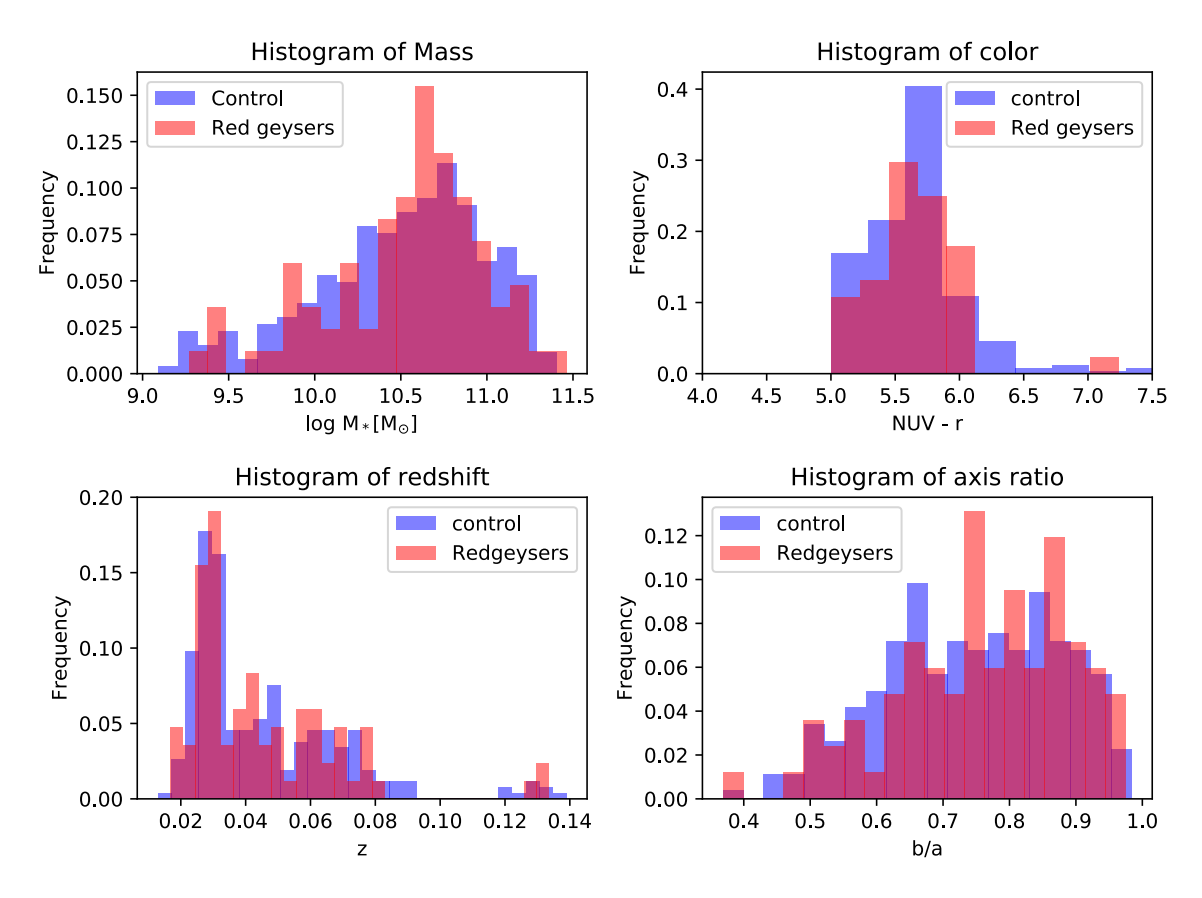


Figure 4. The comparison of global properties of red geysers with our chosen control sample. Normalized histograms of the red geysers and control galaxies in: stellar mass ($\log M_*$), rest-frame NUV-r color, redshift (z), and axis ratio (b/a). The red geyser sample distribution are shown in red, while the control sample properties are shown in blue. We see similar distribution for red geysers and control sample properties, as expected from our method of selection of control sample.

Worthey, G., Faber, S. M., & Gonzalez, J. J. 1992, ApJ, 398, 69 Worthey, G., Tang, B., & Serven, J. 2014, ApJ, 783, 20 Wright, E. L., Eisenhardt, P. R. M., Mainzer, A. K., et al. 2010, AJ, 140, 1868-1881

Yan, R., & Blanton, M. R. 2012, ApJ, 747, 61 Yan, L., Donoso, E., Tsai, C.-W., et al. 2013, AJ, 145, 55 Yan, R., Bundy, K., Law, D. R., et al. 2016, AJ, 152, 197 Yang, X., Mo, H. J., van den Bosch, F. C., et al. 2007, ApJ, 671, 153 York, D. G., Adelman, J., Anderson, J. E., Jr., et al. 2000, AJ, 120, 1579 Young, L. M., Bureau, M., Davis, T. A., et al. 2011, MNRAS, 414, 940 Young, L. M., Scott, N., Serra, P., et al. 2014, MNRAS, 444, 3408 York, D. G., Adelman, J., Anderson, J. E., Jr., et al. 2000, AJ, 120, 1579 Yuan, F., & Narayan, R. 2014, ARA&A, 52, 529 Zensus, J. A. 1997, ARA&A, 35, 607

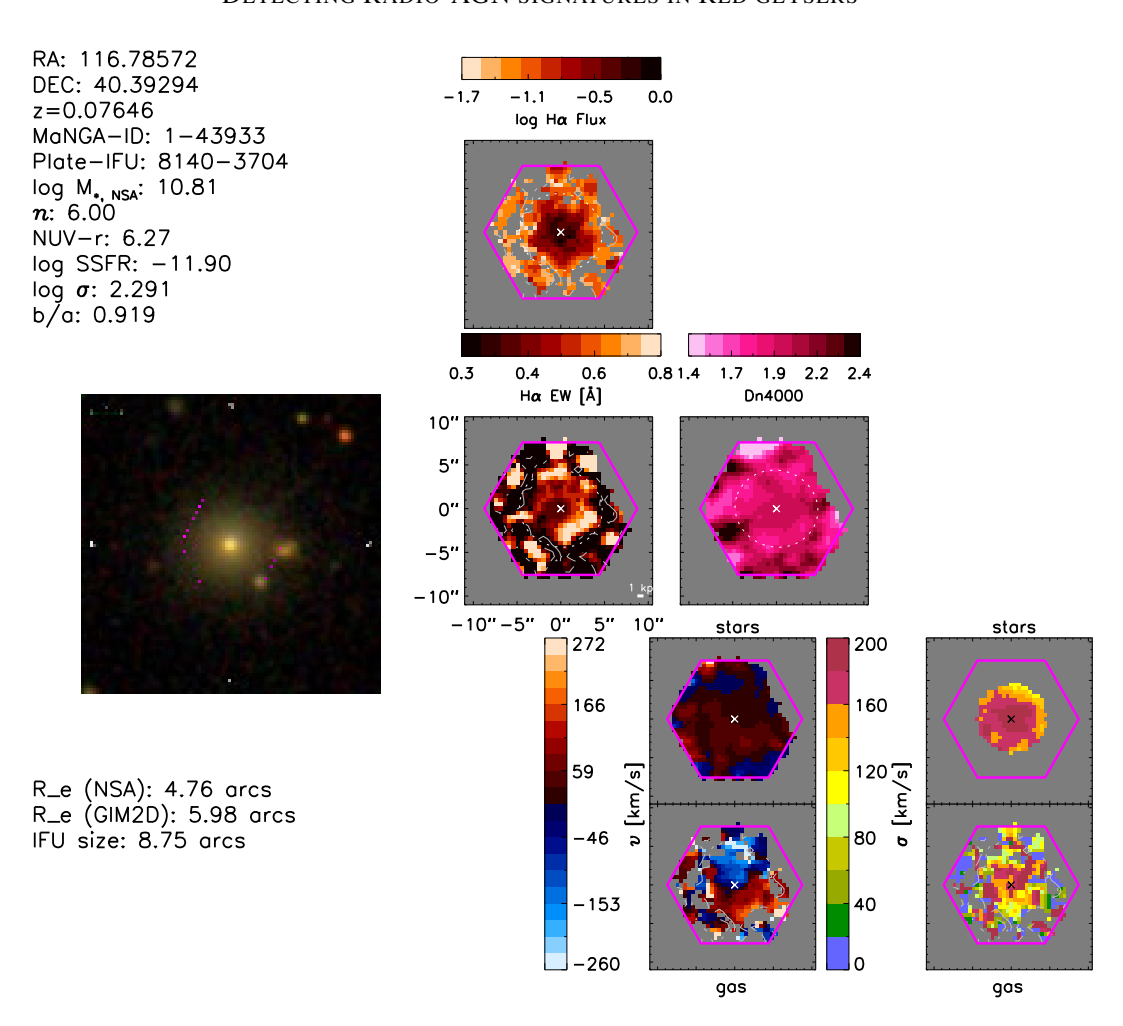


Figure 5. A typical disturbed galaxy as described in §3.1.3. The data has been obtained from MaNGA Integral Field spectroscopic observations. The panel on the left shows the optical image of the galaxy (MaNGA-ID: 1-43933). The magenta hexagon marked in the image is the extent of the MaNGA fiber bundle. On the right, as labelled, we have shown the Hα-flux map, Equivalent width map, Dn4000 absorption map, the velocity maps of gas and the stars along with their dispersion. As described in §3.1.3, this galaxy cannot be called a promising geyser candidate because of the lack of the signature bisymmetric pattern, but the kinematics indicate a difference from ordinary control sample. It has been classified as a third "Hα-disturbed" category to separate from the geyser and the control sample population

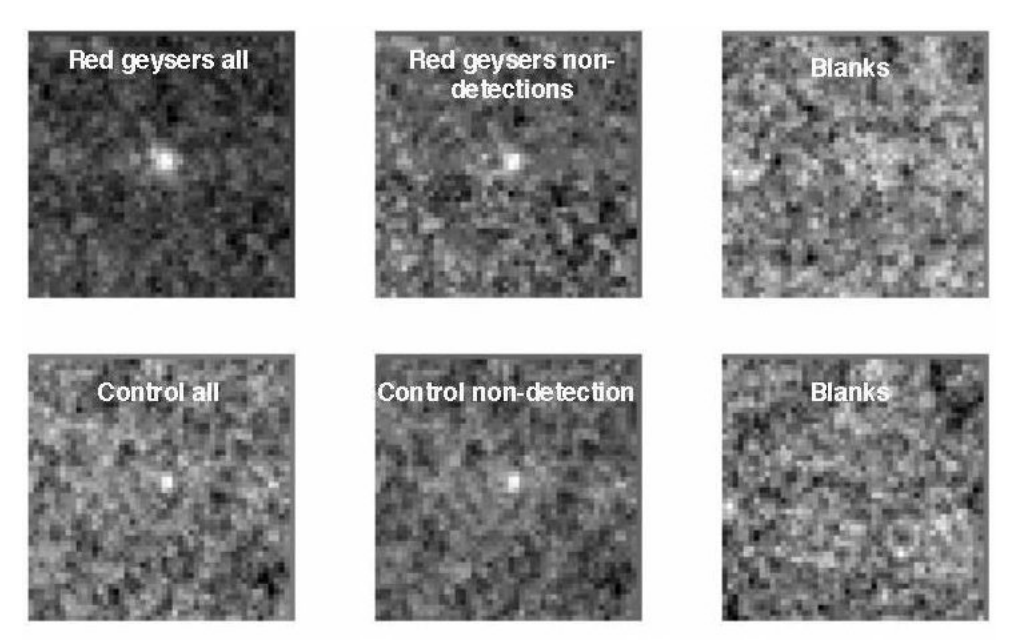


Figure 6. The median stacked images of red geysers (top) and control sample (bottom). The middle panels show the non-radio detected stacked images for the red geysers (middle) and the control (bottom middle), where all radio detected sources have been excluded. The blank stacks are shown in (top right) and (bottom right) panels.

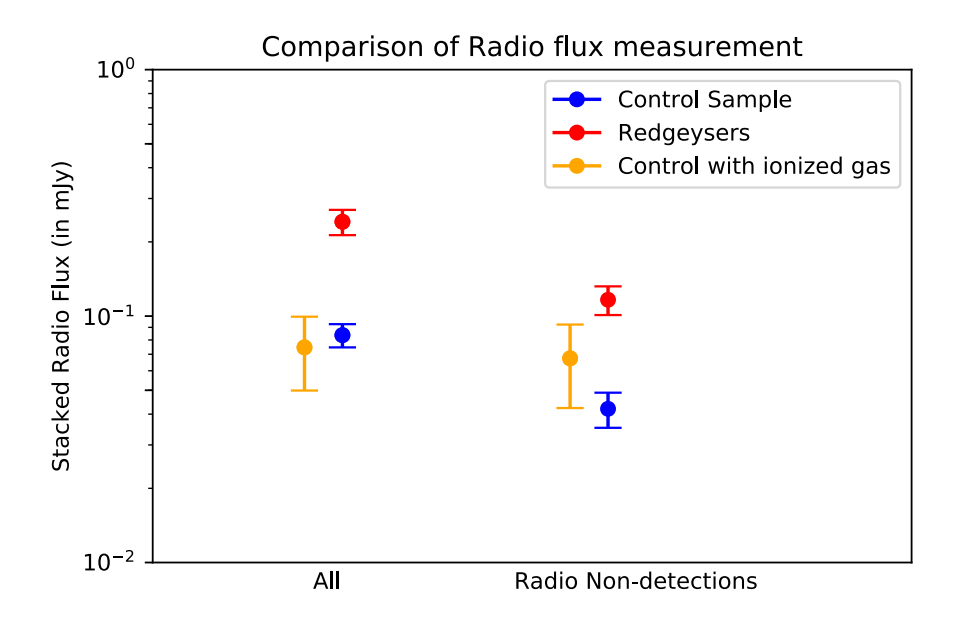


Figure 7. The median stacked radio flux obtained from the stacked sample of red geysers (shown in red) and control sample (blue). This is a one-dimensional plot with x-axis showing the sample included in the stacks and the y value giving the median radio flux of the stacked sample with 1σ errorbars. Here, in the left panel, "All" represents the stacks where the entire sample has been included for both red geysers and control, while "Radio Non-detections" indicate the stacks where the individually radio-detected sources have been removed. The condition of radio detection of a source has been defined as $\frac{flux}{error} > 3$. "Control with gas" – marked in yellow– shows a specific subset of control galaxies when we additionally controlled for ionized gas. As described in §4, control sample has been subdivided based on the H α -EW value— "Control with gas" are the ones with mean H α -EW > 0.5 Å and possibly having a higher amount of gas content in the galaxy than an average quiescent galaxy. The red geyser galaxies have a high EW value (median value ~ 0.8 Å) and therefore a large gas content by definition. It is seen that even the control galaxies with an appreciable amount of ionized gas is well below the stacked signal from the red geysers (red points). The stacked radio flux for the control galaxies with ionized gas (yellow filled circles) doesn't show much difference for "All" and "Radio Non-detections" sample, which information have been obtained from the MaNGA DAP (Data analysis Pipeline) and they have been averaged over the spatial extent of 1.5 effective radii to obtain the mean EW value for a particular galaxy.

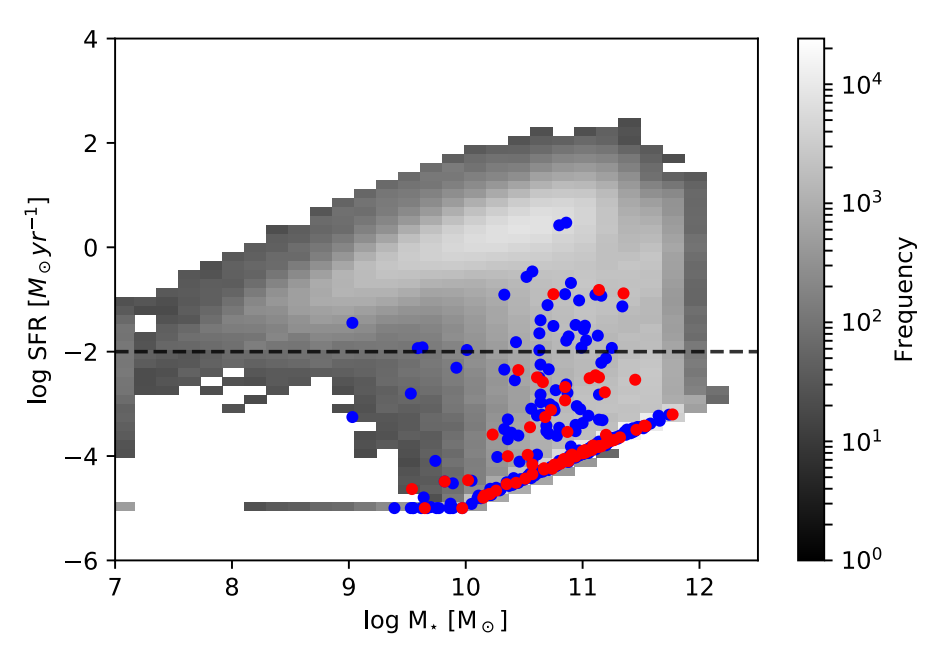


Figure 8. The figure shows the log SFR vs log M_{\star} as obtained from SDSS+WISE catalog of Chang et al. (2015). The grey 2D histogram shows all the galaxies in the catalog with 0.01 < z < 0.1. The points in red and blue signifies red geyser and control sample galaxies respectively. Most of the galaxies in our chosen sample have a low log SFR value, $< -2 \ M\odot/yr$.

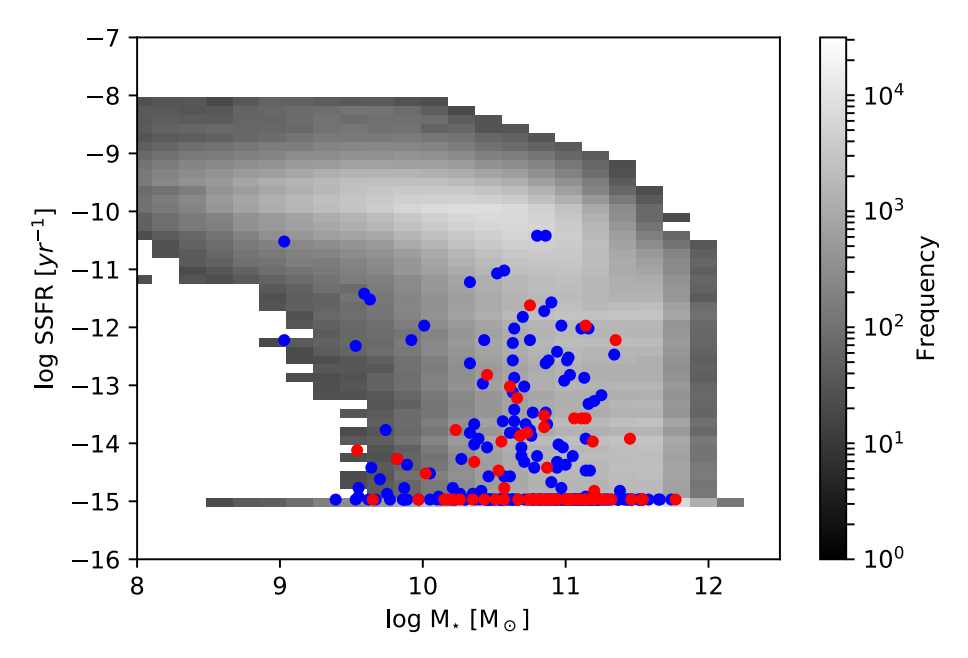


Figure 9. The figure shows the log sSFR vs log M_{\star} as obtained from SDSS+WISE catalog of Chang et al. (2015). The grey 2D histogram shows all the galaxies in the catalog with 0.01 < z < 0.1. The points in red and blue signifies red geyser and control sample galaxies respectively. Most of the galaxies in our chosen sample have a low log sSFR value, $< -12 \text{ yr}^{-1}$.

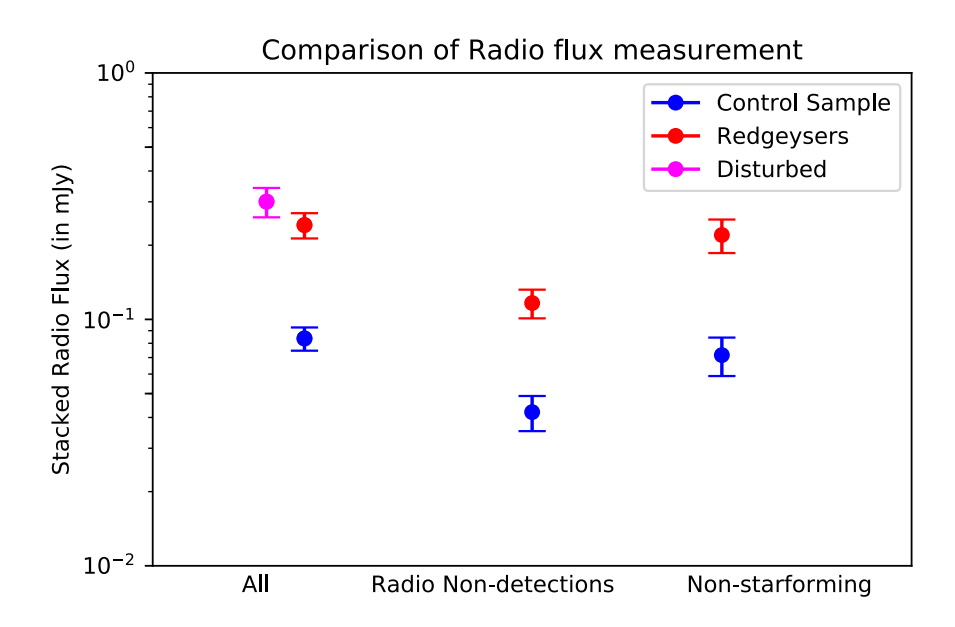


Figure 10. The median stacked radio flux obtained from the stacked sample of red geysers (shown in red), $H\alpha$ -disturbed (pink) and control sample (blue). This is a one-dimensional plot with x-axis showing the sample included in the stacks and the y value giving the median radio flux of the stacked sample with 1σ errorbars. The leftmost panel shows the stacks for the entire sample of red geysers (shown in red), control sample (shown in blue) and the $H\alpha$ -disturbed category (shown in magenta). "Radio Non-detections" panel shows the stacked radio flux for the geysers and the control sample where the individually radio-bright ones, satisfying the criteria $\frac{flux}{error} > 3$, have been removed. The red geyser and the control sample have been cross-matched with SDSS+WISE catalog of Chang et al. (2015). Galaxies with log SFR $> -2M \odot$ /yr have been removed and re-stacked. They constitute the "Non-Starforming" category shown in the rightmost panel of the plot. In all the cases, the median stacked radio flux is higher for the red geyser sample compared to the control sample by $> 5\sigma$.

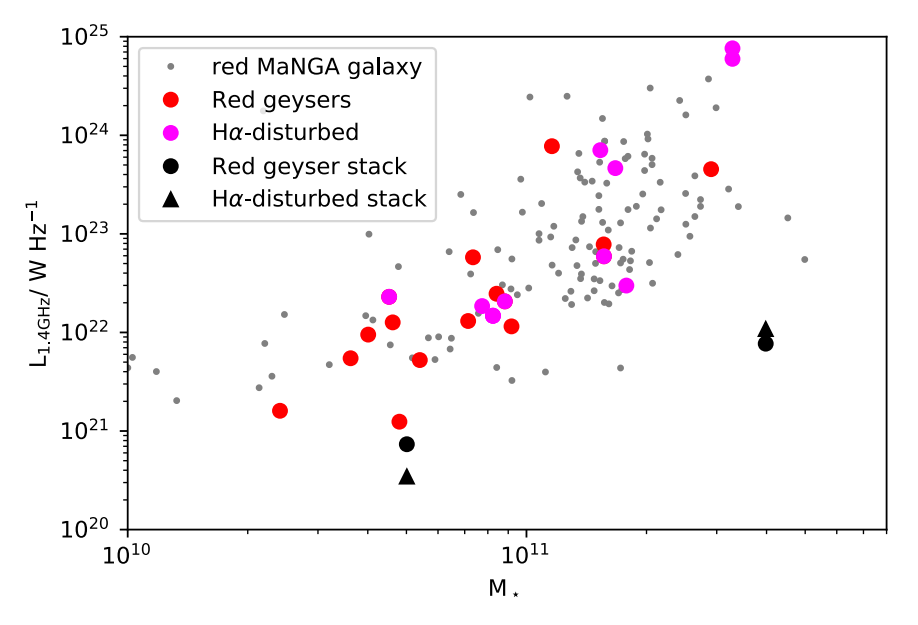


Figure 11. The figure shows the 1.4GHz radio luminosity versus stellar mass of "radio detected" red geysers (shown in red), $H\alpha$ -disturbed (shown in pink) and the red (NUV-r > 5) MaNGA galaxies (in gray). This plot shows that the radio AGN population occupies two distinct regions in the luminosity stellar-mass space depending on the types of host quiescent galaxies. The lower mass regime is occupied by quiescent galaxies with optical emission line features (red geysers and $H\alpha$ -disturbed) while in the higher mass region, we mainly find galaxies without detectable emission line features (similar to our control sample). The black circles and triangles show the stacked radio luminosities from the entire sample (which includes both radio-detected and non-detected ones) of red geyser and $H\alpha$ -disturbed galaxies respectively, in two mass bins.